Journal of Geophysical Research: Oceans

RESEARCH ARTICLE
10.1029/2018JC014027

Three-Dimensional Turbulence-Resolving Simulations of the Plunge Phenomenon in a Tilted Channel

F. N. Schuch[1], L. C. Pinto[1,2], J. H. Silvestrini[1], and S. Laizet[3]

[1]Laboratório de Simulação de Escoamentos Turbulentos, Escola Politécnica, Pontifícia Universidade Católica do Rio Grande do Sul, Porto Alegre, Brazil, [2]Departamento de Engenharia Sanitária e Ambiental, Universidade Federal de Santa Maria, Rio Grande do Sul, Brazil, [3]Department of Aeronautics, Imperial College London, London, UK

Key Points:
- A new framework for turbulence-resolving simulations of an hyperpycnal flow at the bottom floor of a tilted channel is proposed
- This study focuses on the plunge phenomenon
- Good agreement with experimental data generated with the same setup and available analytical models is found

Supporting Information:
- Data Set S1
- Data Set S2
- Data Set S3
- Data Set S4
- Data Set S5
- Data Set S6

Correspondence to:
S. Laizet,
s.laizet@imperial.ac.uk

Citation:
Schuch, F. N., Pinto, L. C., Silvestrini, J. H., & Laizet, S. (2018). Three-dimensional turbulence-resolving simulations of the plunge phenomenon in a tilted channel. *Journal of Geophysical Research: Oceans*, *123*. https://doi.org/10.1029/2018JC014027

Received 29 MAR 2018
Accepted 5 JUN 2018
Accepted article online 12 JUN 2018

Abstract Hyperpycnal flows are produced when the density of a fluid flowing in a relatively quiescent basin is greater than the density of the fluid in the basin. The density differences can be due to the difference in temperatures, salinity, turbidity, concentration, or a combination of them. When the inflow momentum diminishes, the inflowing fluid eventually plunges under the basin fluid and flows along the bottom floor as an underflow density current. In the present work, 3-D turbulence-resolving simulations are performed for an hyperpycnal flow evolving at the bottom floor of a tilted channel. Using advanced numerical techniques designed for supercomputers, the incompressible Navier-Stokes and transport equations are solved to reproduce numerically the experiments of Lamb et al. (2010, https://doi.org/10.1130/B30125.1) obtained inside a flume with a long tilted ramp. This study focuses on presenting and validating a new numerical framework for the correct reproduction and analysis of the plunge phenomenon and its associated flow features. A very good agreement is found between the experimental data of Lamb et al. (2010), the analytical models of Parker and Toniolo (2007, https://doi.org/10.1061/(ASCE)0733-9429(2007)133:6(690)), and the present turbulence-resolving simulations. The mixing process between the ambient fluid and the underflow density current is also analyzed thanks to visualizations of vortical structures at the interface.

1. Introduction

Hyperpycnal flows are a major mechanism for the transport of fluvial, littoral, and shelf sediments into deeper waters (Garcia, 1994). Nearly a third of inland rain precipitation is transported from river to the oceans, according to the annual water cycle study from Trenberth et al. (2007). McCool and Parsons (2004) estimated that 10×10^9 m^3 of sediment are transported from rivers to the oceans every year. Marine ecosystems can be strongly affected by mixing at river mouth due to differences in temperature and salinity, besides sedimentary material in suspension or even pollution spreading (Horner-Devine et al., 2015). The sediment transport by underflow density currents is the foremost mechanism that forms oceanic sedimentary basins, causing deposit, erosion, and even material resuspension from the ocean bed. The resulting deposits can eventually become appropriate hydrocarbon reservoirs of great interest to industry (Meiburg & Kneller, 2010). Furthermore, the deposition of sedimentary material transported from rivers into oceans (hyperpycnites) can potentially preserve an essential record across a variety of climatic and tectonic settings (Mulder et al., 2003) and can be connected to river-flood dynamics (Lamb & Mohrig, 2009). The analysis of hyperpycnal flows is also of great relevance for water quality management in reservoirs as they carry suspended matters and dissolved solids across the reservoir. Consequently, they often determine the distribution of pollutant substances (Bournet et al., 1999).

Hyperpycnal flows are difficult to survey and assess in nature. In the past, hyperpycnal flows entering a basin have been extensively studied theoretically with the development of empirical and analytical models to predict their main features as well as with laboratory experiments at a fairly small scale. Only very few studies are based on numerical simulations. In particular, the understanding of the parameters and mechanisms that govern the flow transition in the plunge zone has motivated several studies over the last five decades. Using 2-D laboratory experiments, Singh and Shah (1971) established an empirical correlation between the depth at the plunge point and initial flow and density difference conditions. These experiments included visual observations of the process of formation of the plunge point and some measurements for the location

of the plunge point, depth of water at the plunge point, inflow discharge, and density characteristics of the underflow current. This experimental study also provided information related to the deposition process along the reservoir and its link with the plunging phenomenon. Savage and Brimberg (1975) presented two analyses of the plunging phenomenon: one based on an energy flow conservation analysis and one based on the analysis of a gradually varied two-layer system. The authors obtained various relations for the depth at the plunge point as well as profiles at the interface between the underflow density current and the ambient fluid from an analysis similar to the one use for an hydraulic jump setup. They used the laboratory experiments of Singh and Shah (1971) for comparisons. A theoretical analysis of a 2-D buoyant flow from a shallow channel into a reservoir with a tilted slope was performed in Akiyama and Stefan (1984). The objective of this work was to study the plunging phenomenon and the prediction of the depth of the plunge point. Several parameters were investigated such as the inflow Froude number, the bed slope angle, the mixing rate, and the total friction coefficient. The data obtained from the equations developed in this study were found to be in good agreement with laboratory and field data. However, a mistake was found in that study for the evaluation of the Froude number when the slope of the bed is changed and a corrected formulation was provided in Parker and Toniolo (2007). The main new result is that the ratio of the underflow thickness just after the plunging point to the depth just before the plunging point, and the associated densimetric Froude numbers can be specified as a function of a single parameter linked to entrainment of ambient fluid into the underflow current. Corrections of the analytical work of Akiyama and Stefan (1984) were also proposed in Dai and García (2009) in order to account for various conditions not addressed in the original study. The main improvement was related to a new formulation for the mixing parameters. About 25 years ago, a review was carried out in Alavian et al. (1992) to discuss about the knowledge of density currents caused by negatively (dense) or positively (light) buoyant flows entering stratified or unstratified lakes and reservoirs. The authors concluded that large-scale experiments and well-defined field studies in simple geometries are crucially needed as well as numerical models in order to better understand the link between the large-scale behavior of underflow density currents and localized turbulent processes.

An experimental investigation of the behavior of a salt solution released down a sloping surface in a tank of freshwater was carried out in Alavian (1986). The main findings of this study are related to the influence of the angle of the sloping surface on the formation of the underflow density current and on theimportance of steep slopes for entrainment. In Lee and Yu (1997), a series of experiments were conducted in a flume to study the hydraulic characteristics of a turbidity current in a reservoir. It was found that the incipient plunge occurred when the densimetric Froude number is equal to unity and that it migrates downstream and finally reached a stable condition when the densimetric Froude number reaches 0.6. It should be pointed out that this quasi steady state Froude number depends mostly on the slope (and bed roughness and size of sediment in suspension), as explain in Sequeiros (2012). Several laboratory experiments in a flume with a tilted slope were performed in Sequeiros et al. (2009) to study the self-acceleration of the head of a turbidity current. Some of these experiments focused on the plunging phenomenon using a sediment-water mixture released near the water surface. The measured head velocities and suspended sediment concentrations were used to calculate a densimetric Froude number for the head of the current and for some parameters a roughly constant densimetric Froude number was maintained for the head of the current, slightly smaller than unity. Note that the Froude number of the body of the turbidity currents in Sequeiros et al. (2009), once the head has passed away, was >1 (e.g., supercritical), which is expected in bed slopes steeper than about 1% as explained in Sequeiros (2012). A layer-averaged integral model for underflow turbidity currents was presented in Garcia (1994) along with laboratory experiments conducted to test several assumptions involved in the model development. The laboratory observations were reproduced fairly well by the model. The author made some connections with an hydraulic jump setup and showed that their proposed model can be used to estimate the distribution of sediment brought in by river inflows into lakes and reservoirs. A very complete and detailed experimental study was performed in Lamb et al. (2010) with the aim to investigate if deposits from the underflow density current can accurately record the rising and falling discharge of a flooding river (in terms of sediment-size grading and deposit thickness). Coarse sediment (sand) were found to be able to record flow accelerations and decelerations related to the plunge phenomenon. In contrast, fine sediment (mud) were found to be relatively insensitive to local plunge point dynamics. Lamb et al. (2010) also noticed that the necessary fluvial sediment concentration to form a plunging plume can be much larger than the concentration typically used in previous studies because of deposition upstream of the plunge point.

Several numerical studies have been published with a focus on plunging density currents. The vast majority of these studies are based on Reynolds-averaged Navier-Stokes (RANS) simulations, most of them in a 2-D setup, using the well-known k-ϵ model (Launder & Spalding, 1972). To the best of our knowledge, 3-D turbulence-resolving simulations have not yet been performed for the study of an hyperpycnal flow evolving at the bottom floor of a tilted channel. The 2-D RANS simulations were performed in Farrell and Stefan (1988) to study the flow into and through a reservoir with a sloping bottom for a wide range of flow conditions and bottom slopes. The numerically generated plunge depths followed the expected trend, but the actual plunge depth values were found to be larger than the experimentally determined values. Initial entrainment values in the plunging region were also computed and found to be of the same order of magnitude as the measured values. A numerical investigation to study the plunging phenomenon and associated entrainment both in a sloping and a diverging channel was performed in Bournet et al. (1999). Calculations of the entrainment as well as of the plunge properties were achieved and compared with various models of the literature. An analysis of the plunging phenomenon in dam reservoirs using 3-D RANS simulations was carried out in Üneş (2008, 2010). The effect of inflow conditions including varying density and temperature, Froude number of the inflow, and sloping bottom inclination was investigated, and the Coriolis force effect was taken into account. The authors found a good agreement with experimental data. The potential of an artificial neural network approach was also investigated by the same authors for the prediction of density flow plunging depth in dam reservoirs. The 3-D RANS simulations of turbid underflows generated by the plunging of a river were performed in Kassem and Imran (2001) and Kassem et al. (2003) using an original approach based on the splitting of the current into different single flow processes. The successful implementation of this model in laboratory and field cases provided new insights on the dynamics of underflow turbidity currents with a particular focus on the transformation of a river flow into a negatively buoyant plume. Numerical simulations of hyperpycnal events have been conducted in Khan et al. (2005) using a 2-D depth-integrated finite volume model in order to solve the depth-averaged equation of mass, momentum, and sediment conservation of density driven flow along with the Exner equation of bed sediment continuity. The results indicated that the current in the ambient fluid can have a great impact on the spreading and deposition pattern of the hyperpycnal flow. Sedimentary deposits generated from a series of simulated hyperpycnal flow events were found to develop undulating bed forms. A coupled 3-D hydrodynamics and 2-D underflow model was proposed in Dallimore et al. (2004) for simulations of the plunge phenomenon in reservoirs with a constant width and slope. The resulting plunge depths were found to be in agreement with prior empirical models. Comparisons were also made with field data with a good agreement between field and model results. More recently, Dai et al. (2007) performed large eddy simulations (LES) of a plunging flow in a 2-D channel to investigate the dynamics in the plunge region with a focus on the mixing properties of the flow.

The main objective of this work is to propose a new framework for the study of polydisperse hyperpycnal flows based on turbulence-resolving simulations. In order to benchmark this numerical framework, the simulations are performed with the same experimental setup as Lamb et al. (2010) and the analytical models of Parker and Toniolo (2007) are used for validation purposes. The plunge phenomenon and its associated features observed in nature are very complex, very voluminous, and are extremely challenging and costly to study. As a result, they are mainly investigated in very simplified and idealized configurations in lab-scale experiments or with simplified numerical models. Three-dimensional turbulence-resolving simulations are not yet feasible for large-scale plunge flows. At the moment, our aim is to be able to reproduce lab-scale experiments for which the Reynolds number is 2 or 3 orders of magnitude smaller that those observed in nature. The manuscript is organized in six sections: an introduction, a description of governing equations, computational setup, and the numerical methods behind the new framework, a result section based on four turbulence-resolving simulations, and a conclusion.

2. Governing Equations

The proposed new framework is based on the resolution of the incompressible Navier-Stokes equations. For the present study, three scalar transport equations under the Boussinesq approximation are used for sediments with three different particles sizes. The incompressible Navier-Stokes equations are written in their dimensionless form as

$$\frac{\partial u_j}{\partial x_j} = 0, \tag{1a}$$

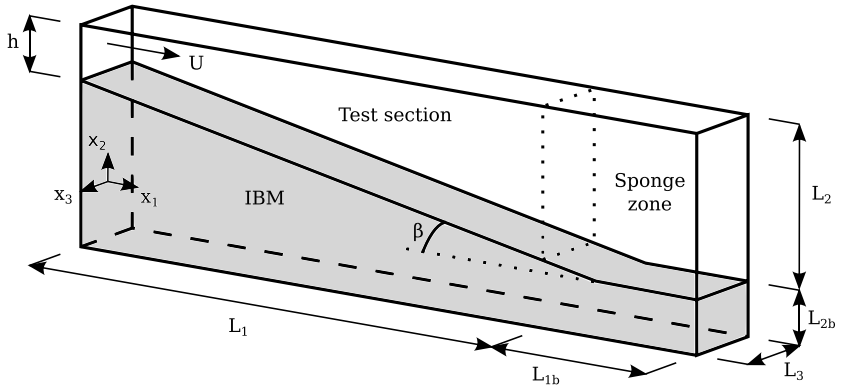

Figure 1. Schematic representation of the computational domain (not to scale). IBM = immersed boundary method.

$$\frac{\partial u_i}{\partial t} + u_j \frac{\partial u_i}{\partial x_j} = -\frac{\partial p}{\partial x_i} + \frac{1}{Re} \frac{\partial^2 u_i}{\partial x_j \partial x_j} + e^g \frac{1}{Fr^2} \sum_{i=1}^{3} c_i, \tag{1b}$$

$$\frac{\partial c_i}{\partial t} + \left(u_j + u_i^s e^g\right) \frac{\partial c_i}{\partial x_j} = \frac{1}{ReSc} \frac{\partial^2 c_i}{\partial x_j \partial x_j}, \qquad i = 1, \ldots, 3, \tag{1c}$$

where u_i, p, and c_i correspond to velocity, pressure, and portion of each particle size, respectively, together with the coordinate system x_i (see Figure 1), time t, and unit vector pointing in gravity direction $e^g = [0, -1, 0]$. u_i^s is the settling velocity for each particles size, which may be considered constant. It is related to the particle diameter by the Stokes settling velocity law (Julien, 2010), which assumes that the dominant flow force on an individual particle is the Stokes drag. The Reynolds, densimetric Froude and Schmidt numbers at the inlet, and the Stokes settling velocity are the four dimensionless parameters defined as follows:

$$Re = \frac{\tilde{q}_0}{\tilde{\nu}}, \tag{2a}$$

$$Fr = \frac{\tilde{q}_0}{\sqrt{R\tilde{C}_r \tilde{g} \tilde{h}^3}}, \tag{2b}$$

$$Sc = \frac{\tilde{\nu}}{\tilde{D}}, \tag{2c}$$

$$u_i^s = \frac{\tilde{u}_i^s \tilde{h}}{\tilde{q}_0} = \frac{\tilde{d}_i^2 R \tilde{g} \tilde{h}}{18 \tilde{\nu} \tilde{q}_0}, \tag{2d}$$

where $\tilde{\cdot}$ corresponds to dimensional quantities. $\tilde{q}_0$ is the volumetric discharge per unit width defined as the ratio of the inlet velocity $\tilde{U}_0$ with the length $\tilde{h}$. The kinematic viscosity is $\tilde{\nu}$, the fresh water and sediment densities are $\tilde{\rho}_w$, $\tilde{\rho}_p$, with R defined as $(\tilde{\rho}_p - \tilde{\rho}_w)/\tilde{\rho}_w$. The gravity acceleration is $\tilde{g}$, the constant diffusivity of particle concentration is $\tilde{D}$ and the particle diameter $\tilde{d}_i$. All parameters and variables are made dimensionless using the influx velocity $\tilde{U}_0$, depth $\tilde{h}$, and sediment concentration $\tilde{C}_r$ (associated dimensionless parameters are h, U_0, and c_t).

3. Computational Setup

The computational domain, shown in Figure 1 (not to scale), can be divided into three sections. Highlighted in gray, the bed slope with declivity $S = \tan(\beta)$ is inserted in the computational domain using an immersed boundary method based on the alternating direction forcing strategy introduced by Gautier et al. (2014). A L_{1b} streamwise long sponge zone is implemented only at the very end of the computational domain to reduce the turbulence levels without reducing the streamwise velocity, and, to avoid any numerical instabilities at the outlet. This sponge zone is defined using the absorption coefficient:

$$\sigma_{ab}(x_1) = \frac{1}{2}\left[1 - \tanh(x_1 - L_1 - L_{1b} + 3)\right], \tag{3}$$

in order to promote a full sedimentation of particles before the current reaches the outflow boundary condition and to remove negative velocity at the boundary. This numerical approach mimics the forced sedimentation commonly used downstream of a test section in laboratory experiments. The inflexion point of the hyperbolic tangent is located $3h$ upstream of the outlet boundary condition. Preliminaries studies have shown that the use of a sponge zone significantly decreases computational costs by allowing the reduction of the domain length in the streamwise direction. Note that the conservation of mass is not satisfied in the sponge zone but it does not affect the test section, where all the data presented in the manuscript are computed. Furthermore, a L_{2b} height immersed boundary method layer equal to h is used to guarantee the correct solid-fluid boundary conditions downstream of the test section where all statistics presented in this paper are calculated.

The following inflow profiles are used for the velocity and for the concentration at the inlet boundary condition:

$$c_i(0, x_2, x_3) = G(x_2)c_{0i}, \tag{4a}$$

$$u_i(0, x_2, x_3) = [G(x_2), 0, 0], \tag{4b}$$

with

$$G(x_2) = \begin{cases} \tanh\left\{\frac{\sqrt{\pi}}{\delta_h}[x_2 - L_2 + h + A \cdot \sin(t)]\right\} & \text{if } x_2 > L_2 - h, \\ 0 & \text{if } x_2 \le L_2 - h. \end{cases} \tag{5}$$

$\delta_h = 0.01$ corresponds to the shear layer thickness of the tangent hyperbolic profiles and c_{0i} to the inlet portion of each particle size. The sinusoidal term with amplitude $A = 0.005$ is designed to trigger instabilities at the inlet boundary condition. Conventional 1-D convection equations are used at the outlet boundary condition ($x_1 = L_1 + L_{1b}$) for the concentration of particles and for the velocity:

$$\frac{\partial c_i(L_1 + L_{1b}, x_2, x_3)}{\partial t} + U_c \frac{\partial c_i(L_1 + L_{1b}, x_2, x_3)}{\partial x_1} = 0 \tag{6a}$$

$$\frac{\partial u_i(L_1 + L_{1b}, x_2, x_3)}{\partial t} + U_c \frac{\partial u_i(L_1 + L_{1b}, x_2, x_3)}{\partial x_j} = 0 \tag{6b}$$

U_c represents the advective velocity normal to the outlet boundary condition and is equal to unity. For the top vertical boundary condition ($x_2 = L_2$) a nondeformable water surface is assumed, which according to Nasr-Azadani et al. (2013) is best described by a no-flux boundary condition for the particle concentration and a free-slip boundary condition for the carrier fluid:

$$\frac{1}{ReSc}\frac{\partial c_i(x_1, L_2, x_3)}{\partial x_2} - u_i^s c_i(x_1, L_2, x_3) = 0, \tag{7a}$$

$$\left[\frac{\partial u_1(x_1, L_2, x_3)}{\partial x_2}, u_2(x_1, L_2, x_3), \frac{\partial u_3(x_1, L_2, x_3)}{\partial x_2}\right] = [0, 0, 0]. \tag{7b}$$

At the solid-fluid interface x_{2l} (the bottom floor of the ramp, see Figure 1), the deposition of particles is reproduced with a convective outflow condition for the particles concentration (Necker et al., 2002) and a no-slip boundary condition is used for the velocity:

$$\frac{\partial c_i(x_1, x_{2l}, x_3)}{\partial t} - u_i^s \frac{\partial c_i(x_1, x_{2l}, x_3)}{\partial x_2} = 0, \tag{8a}$$

$$u_i(x_1, x_{2i}, x_3) = [0, 0, 0], \tag{8b}$$

A no-flux boundary condition for the concentration and velocity is applied in the spanwise direction (for $x_3 = \pm L_3/2$):

$$\frac{\partial c_i(x_1, x_2, \pm L_3/2)}{\partial x_3} = 0, \tag{9a}$$

$$\left(\frac{\partial u_1(x_1, x_2, \pm L_3/2)}{\partial x_3}, \frac{\partial u_2(x_1, x_2, \pm L_3/2)}{\partial x_3}, u_3(x_1, x_2, \pm L_3/2)\right) = [0, 0, 0]. \tag{9b}$$

Table 1
Experimental Volumetric Discharge per Unit Width $\tilde{q}_0$ and Volumetric Sediment Concentration $\tilde{C}_r$, From Lamb et al. (2010) Recorded at the Inlet as Well as the Respective Reynolds Number Re, Froude Number Fr, and Stokes Settling Velocity u_i^s for Each Granulometric Fraction

Quantities	4	5	6	7
$\tilde{q}_0$ (m^2/s)	0.0025	0.0033	0.0043	0.0043
$\tilde{C}_r$ (%)	0.54	0.54	0.54	1.00
Re	2500	3300	4300	4300
Fr	8.45	11.16	14.54	10.68
$u_1^s \times 10^{-5}$	3.2	2.5	1.9	1.9
$u_2^s \times 10^{-3}$	1.6	1.2	0.9	0.9
$u_3^s \times 10^{-3}$	6.7	5.0	3.9	3.9

The configuration of the present numerical simulations aims to reproduce the experimental channel setup of Lamb et al. (2010). The test section dimensions ($L_1 \times L_2 \times L_3$) are equal to ($250h \times 15.875h \times 4h$), and the ramp declivity is equal to $S = 0.05$. Note that the spanwise test section extent is 6 times smaller in the present study by comparison to the experimental setup of Lamb et al. (2010) due to computational limitation. A preliminary study for case 7 with an even shorter spanwise test section extent equals to $2h$ has shown that the size of the spanwise test section for the present simulations does not affect the quantities presented in the present study. The inlet flow height of the experimental channel, used as reference length unit, is $\tilde{h} = 10$ mm. The total streamwise extend of the full experimental setup ($700h$) is too large to be reproduced in the simulations, hence the use of the sponge zone. The full computational domain for the present simulations ($(L_1 + L_{1b}) \times (L_2 + L_{2b}) \times L_3 = 312.5h \times 16.875h \times 4h$) is discretized using ($n_1 \times n_2 \times n_3$) = ($2,001 \times 241 \times 31$) mesh points, while the time step is equal to $\Delta t = 0.01$.

Seven experiments were carried out by Lamb et al. (2010), and cases 4 to 7 are used in the present study for comparison. The volumetric discharge per unit width $\tilde{q}_0$, the volumetric sediment concentration $\tilde{C}_r$ at the inlet boundary condition, and the Reynolds and Froude numbers and Stokes velocities are presented in Table 1 (the Schmidt number is equal to 1 in the present study). The experimental grain-size distribution of crushed silica, with a density of $\tilde{\rho}_p = 2,650$ kg/m^3, can be reproduced with particles of diameters $\tilde{d}_1 = 3$ μm ($c_{01} = 0.32$), $\tilde{d}_2 = 21$ μm ($c_{02} = 0.36$), and $\tilde{d}_3 = 43$ μm ($c_{03} = 0.32$); see Lamb et al. (2010) for more details. A preliminary study has shown that the use of three different particles sizes does not impact significantly the flow dynamics (i.e., plunge position or velocity and height of the underflow) by comparison to a monodisperse case. However, the present study is based on polydisperse simulations for a more extensive and comprehensive study. Simulations are performed for a total of 5×10^5 iterations, corresponding to an adimensional time of 5,000. The statistics are collected after 3×10^5 iterations.

4. Numerical Methodology

The proposed framework to solve the previous equations for the problem illustrated in Figure 2 using turbulence-resolving simulations is based on the open-source high-order flow solver `Incompact3d` (www.incompact3d.com), which solves the governing equations on a Cartesian mesh. Our approach is based on implicit LES in which only the largest scales of the flow are resolved, providing a direct representation of the energy-containing flow structures. The influence of the small scales, which are not resolved by the simulations, is modeled by adding artificial dissipation when computing the viscous term (Grinstein et al., 2007; Sagaut, 2006). The flow solver `Incompact3d` is based on high-order finite-difference schemes, with a spectral treatment for the Poisson equation using relevant three-dimensional (3-D) fast Fourier transforms (FFTs) and the concept of modified wave numbers (Lele, 1992). The divergence-free condition is ensured up to machine accuracy. The pressure mesh is staggered from the velocity mesh by half a mesh, to avoid spurious pressure oscillations. More details about the numerical methods used in `Incompact3d` can be found in Laizet and Lamballais (2009). For the proposed framework, the version of `Incompact3d` based on a highly scalable 2-D domain decomposition is used in order to run the simulations on supercomputers. The computational domain is split into a number of pencils, which are each assigned to a Message Passing Interface (MPI) process. The derivatives and interpolations in the x direction (y direction and z direction) are performed in X pencils (Y pencils and Z pencils), respectively. The 3-D FFTs required by the Poisson solver are also broken down as series of 1-D FFTs computed in one direction at a time. Global transpositions to switch from one pencil to another are performed with the MPI command `MPI_ALLTOALL(V)`. See Laizet and Li (2011) for a detailed description of this domain decomposition strategy. For the present study, the simulations are performed with 192 computational cores. Each simulation ran for approximately 80 hr on a supercomputer based on Intel Xeon E5645 (2.40 GHz) processors. It should be noted that this wall clock time could easily be reduced by increasing the number of computational cores when running the simulations.

Recently, a new method was developed to control the aliasing errors via the viscous term when high-order finite-difference schemes are used (Dairay et al., 2017; Lamballais et al., 2011). For the present numerical

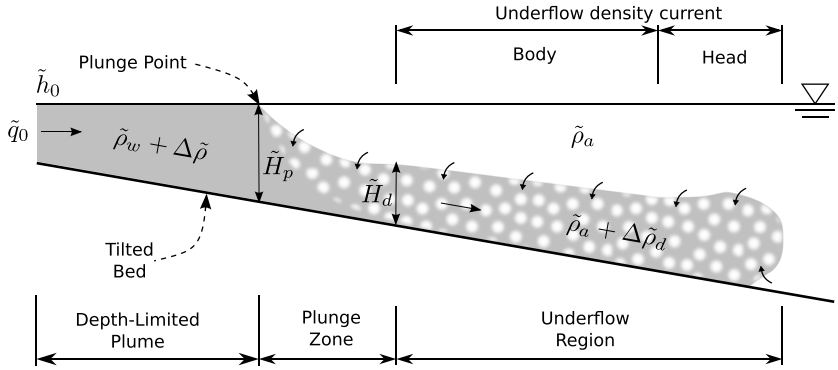

Figure 2. Illustration of an hyperpycnal flow in a tilted channel.

investigation based on turbulence-resolving simulations, this type of schemes was designed to be overdissipative at the highest wave numbers (in the spectral range where even a high-order finite-difference scheme becomes inaccurate), through the use of a less compact formulation that preserves the sixth-order accuracy of the scheme (Dairay et al., 2017; Lamballais et al., 2011).

5. Results

Figure 2 shows the general flow situation under investigation in the present numerical study. The flows can be divided in three regions with distinct characteristics: a depth-limited plume, a plunge region, and an underflow region. At a position determined by a balance between the momentum of the flow and the density difference between the incoming flow and the ambient fluid, a plunge point is forming. Prior to plunging, the flow is momentum dominated (depth-limited plume), while after plunging the density current becomes buoyancy driven (underflow region). The depth-limited plume is located between the inlet boundary condition where the volumetric discharge is constant and the plunge point. At sufficient depth, the flow collapses in the plunge zone and accelerates due to the reduction in flow height. The resulting underflow density current is characterized by an intense turbulent mixing and entrainment, due to an intense turbulence activity at the interface with the ambient fluid.

The temporal evolution of the flow for case 4 can be seen in Figure 3 with instantaneous side view visualizations of the total concentration field c_t at four different times. As expected, it can be seen that the current is spreading down the slope of the tilted channel and the main features reported in Figure 2 can be observed in the present simulations. The head and the body of the underflow current can clearly be seen in the top two visualizations as well as the formation and the initial streamwise evolution of the plunge point, moving from 100*h* to 130*h* downstream of the inlet boundary condition. The bottom two visualizations are presenting a more established flow configuration with a nearly steady plunge point located at $x_1 \approx 165h$ downstream of the inlet boundary condition. Small instabilities under the form of a mixing layer with small coherent vortical structures can be observed in Figure 3 very close to the inlet boundary conditions. They are generated

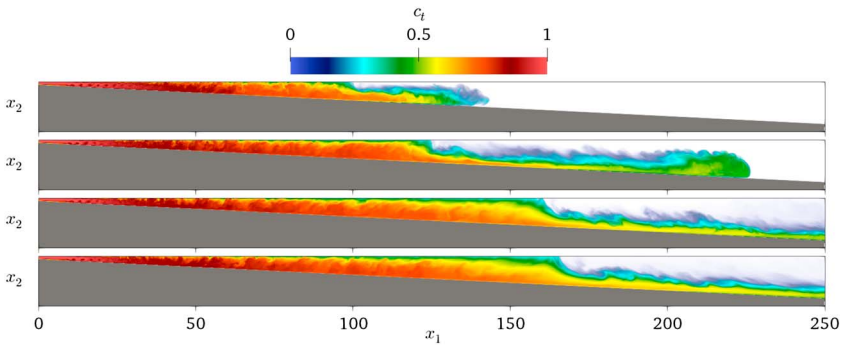

Figure 3. Side view of the total concentration field for case 4 in the test section, for dimensionless time equals to 500, 1,000, 3,000, and 5,000 from top to bottom, respectively.

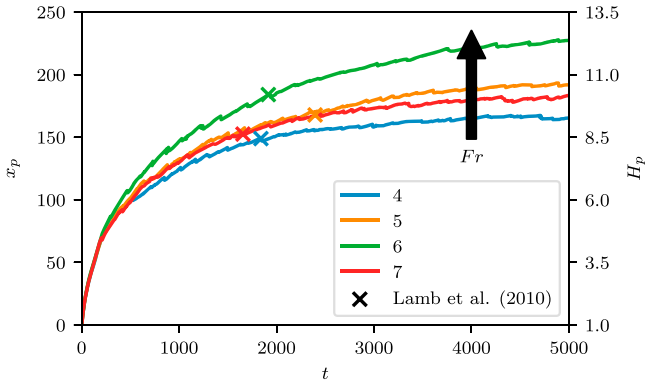

Figure 4. Temporal evolution of the plunge point position x_p and the corresponding channel depth H_p. The X marks indicate the experimental plunge positions obtained for cases 4 to 7 in Lamb et al. (2010).

by the small disturbance imposed numerically at the inlet boundary conditions. The entrainment mechanism at the interface between the ambient fluid and the underflow density current can be visualized with the dark blue color, which corresponds to low concentration levels for the particles. It can be seen that the interface is actually quite large at the top of the body of the underflow density current, which is typical of supercritical flows, a state expected for the present bed slope once the underflow current is well developed away from the plunge point.

The streamwise location of the plunge point x_p is computed as the streamwise length from the inlet boundary condition where the spanwise-averaged total concentration at the top boundary is less than 1%, while H_p represents the corresponding channel depth at this location. The temporal evolution of the plunge point x_p and corresponding channel depth H_p are plotted in Figure 4. The first important result is that the present numerical results seem to be consistent with the experimental reference data even if it seems difficult to reach a perfectly stationary state for the plunge location, except maybe for case 4. It is expected that the position of the plunging point will eventually reach an asymptotic state for all cases but it seems that the computational time for the present simulations is not long enough to attain this asymptotic state. It is particularly evident when the flow rate and Froude number are high (case 6), which suggest that the numerical reproduction of some of the experiments of Lamb et al. (2010) might be challenging for obvious computational cost, especially if a large streamwise and vertical extents combined with a very long wall clock time are needed to get a steady plunge point. The authors in Lamb et al. (2010) observed that the sediments deposition on the bed decreases the channel depth and, as consequence, translates the plunge point downstream by $\sim 20h$ during each experiment. It is not possible to take into account this effect in the present simulations, which could explain why the X marks in Figure 4 are located at a fairly early time when compared to the numerical results. Actually, the X marks indicate when each

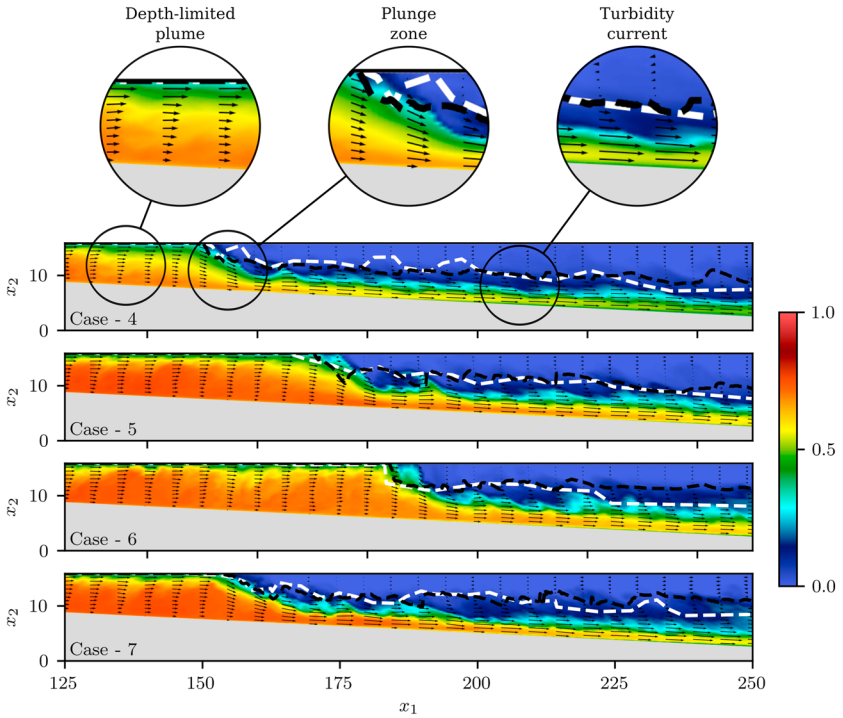

Figure 5. Instantaneous spanwise-averaged visualization of the plunge phenomenon plotted at the time corresponding to the X marks in Figure 4. The arrows indicate velocity direction and magnitude; the concentration field is shown in colors, and the white dashed lines correspond to the experimental data of Lamb et al. (2010) for the elevation profile. The black dashed lines correspond to the present simulations and are obtained with the spanwise-averaged streamwise velocity $u_1 = 10\%$ isoline.

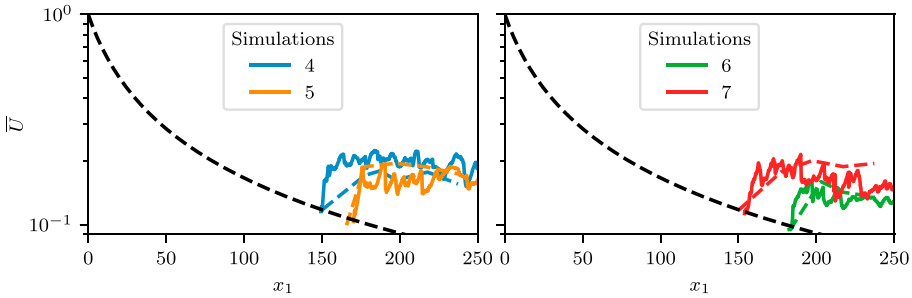

Figure 6. Depth-averaged velocity $\overline{U}$ as function of x_1. The dashed black line corresponds to $\overline{U} = q_0/H$. The dashed colored lines correspond to the experimental data of Lamb et al. (2010).

simulation reaches the experimental plunge location, and the corresponding times are used as reference in Figures 5 and 6 so that comparisons can be made with the same flow depth at the plunge point.

The flow behavior in the three major regions of the flow is presented in Figure 5. The elevation profile corresponds to the interface between the ambient fluid and the underflow current. Experimentally, it is described as an instantaneous concentration isoline (white dashed line in Figure 5). Numerically, it is defined using the spanwise-averaged streamwise velocity $u_1 = 10\%$ isoline (as the streamwise velocity is very small in the ambient fluid and is nonzero in the underflow current). This criterion is more accurate in the simulations than a concentration isoline to defined the depth of the underflow density current and gives better results for comparison with the experimental data of Lamb et al. (2010). The visualization of simulated concentration fields are in good agreement with experimental elevation profiles for all cases, although differences can be observed due to the unsteadiness of the flow at the interface between the current and the ambient fluid. In the depth-limited plume, the velocity vectors, aligned horizontally, are small close to the bottom of the channel (no-slip boundary condition) but are increasing in size when moving close to the top boundary condition (free-slip boundary condition). In the plunge zone, the velocity vectors are inclined toward the bottom of the channel, suggesting that some ambient fluid is entrained in the newly formed underflow density current. In the current, the velocity vectors are fairly long and aligned with the slope of the bottom floor, which suggest that the underflow current is evolving much faster than the inlet incoming flow. Intensity and magnitude of the velocity vectors are changing from one case to another, but these observations are similar for all cases, the only difference being the streamwise location of the plunge point and the thickness of the underflow density current.

The depth-averaged velocity $\overline{U}$ is computed by setting to zero the velocity above the elevation profile in the underflow region in the snapshots showed in Figure 5. Note that the flow discharge is constant upstream of the plunge point ($q_p = q_0$), so the depth-averaged velocity is only a function of the channel's depth $\overline{U} = q_0/H$ in this region. Figure 6 shows a good agreement between the numerical results and experimental data, for both acceleration in the plunge region and the velocity downstream in the underflow density current. As already observed in the experiments of Lamb et al. (2010), the plunge point has a significant influence on the depth-averaged velocity $\overline{U}$. In the depth-limited plume, the flow decelerated gradually, reaching its minimum depth-averaged velocity at the plunge point. Then, a significant acceleration occurs in the plunge region, a trend more pronounced in the numerical data with a nearly vertical profile just downstream of the plunge point. The depth-averaged velocity is nearly doubled in a very short distance. Finally, downstream of the plunging plume, the depth-averaged velocity is nearly constant for all cases.

Figure 7 presents visualization of the concentration field combined with a Q-criterion isosurface $Q = \frac{1}{2}\left(\Omega_{ij}\Omega_{ij} - S_{ij}S_{ij}\right) = 1\%$, defined as a balance between the rotation rate and the strain rate. Such criterion can be used to define a vortical structure as a spatial region. If the rotation rate is larger than the strain rate ($Q > 0$), it means that the vorticity dominates in the flow field. Q isosurfaces are therefore a good indicator of turbulent flow structures (Haller, 2005). Very intense vortices can be observed for all cases just downstream of the plunge zone and at the interface between the underflow density current and the ambient fluid, featuring an intense mixing activity. As expected, it can be noticed that the turbulence activity at the interface between the underflow density current and the ambient fluid is related to the Reynolds number. For case 4, with the lowest Reynolds number, the turbulence has almost vanished at the end of the computational domain. The streamwise extent of the domain after the plunge point in case 4 is longer than for the other cases,

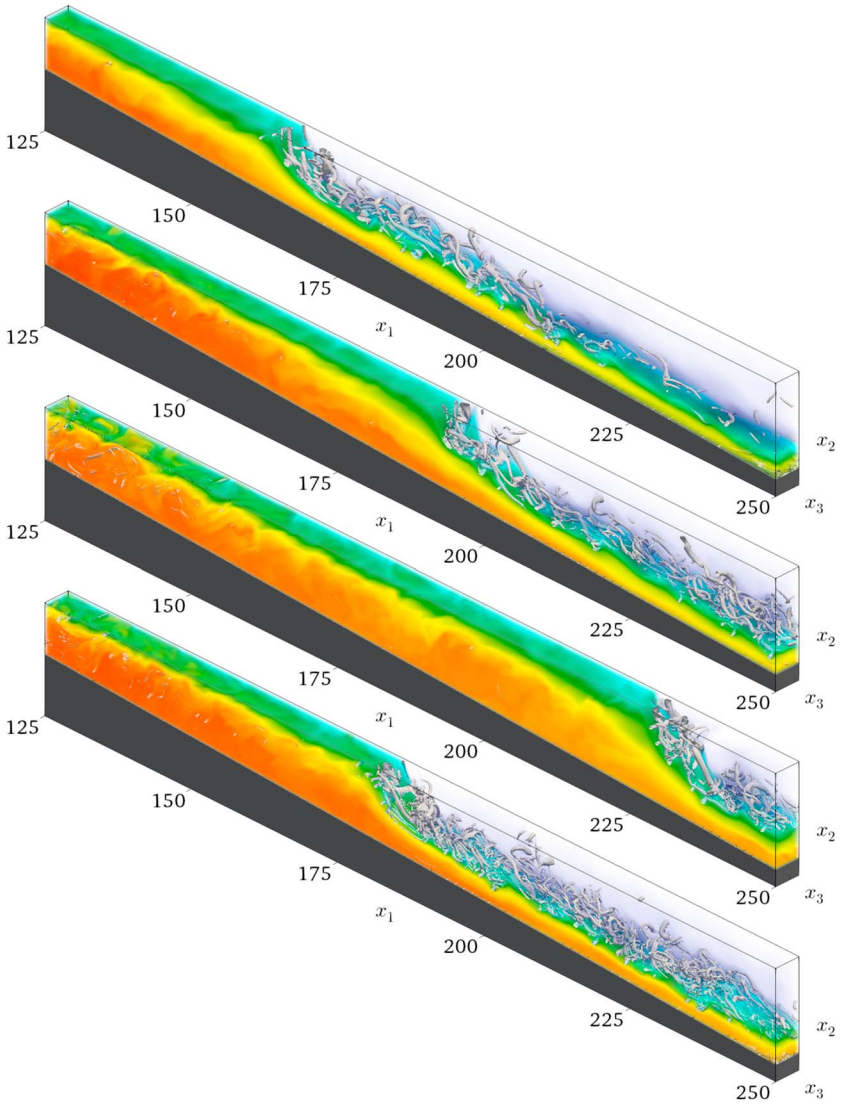

Figure 7. Instantaneous visualizations of the concentration field (same color scheme as in Figure 3), combined with a Q-criterion isosurface ($Q = 1\%$) for cases 4 to 7 from top to bottom, respectively, at $t = 5,000$.

which means that there is a shorter domain for the underflow current to develop for cases 5 to 7. It is therefore not possible to conclude if the turbulence will also vanish for those cases. Another interesting feature is that some vortical structures can be seen close to the top boundary condition in the ambient fluid, suggesting that the mixing process is not necessarily confined at the interface and can expend deep inside the ambient fluid. It can be hypothesized that the entrainment associated with mixing happening at scales as large as the vortical structures (engulfment process) and not just happening at the viscous scales (nibbling process). Engulfment is caused by the large-scale ingestion of the ambient (usually irrotational) fluid, and nibbling is associated to entrainment at viscous scales caused by small-scale vortical motions (da Silva et al., 2014).

The plunge of a hyperpycnal flow such as the one in the present numerical study is only possible when two conditions are satisfied. First, the concentration of particles must be high enough to exceed the ambient fluid density. According to Lamb et al. (2010), this critical concentration $\tilde{c}_c$ can be written as

$$\tilde{c}_c = \frac{1}{R}\left(\frac{\tilde{\rho}_a}{\tilde{\rho}_w} - 1\right), \tag{10}$$

in which it is evident that in the fresh ambient water ($\tilde{\rho}_a = \tilde{\rho}_w$) the critical concentration results in $\tilde{c}_c = 0$. Second, the channel must be deep enough to destabilize the incoming flow. The plunge position for each

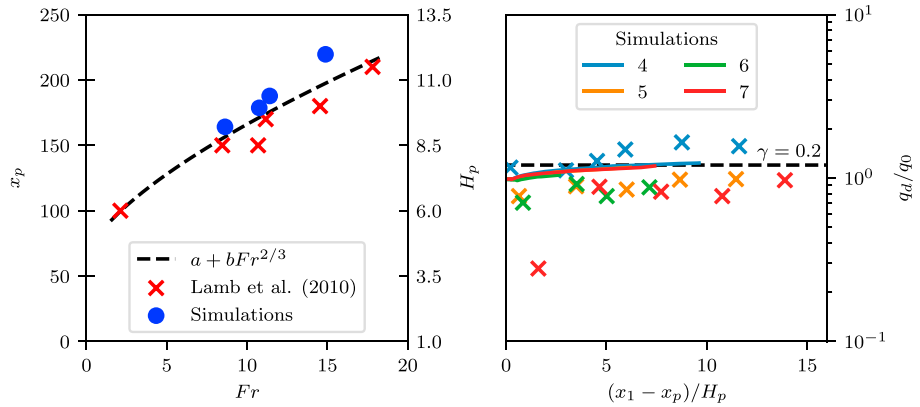

Figure 8. (left) Plunge position and associated flow depth at plunge point versus densimetric Froude number. (right) Discharge of the turbulent current versus distance from plunge point. Points represent experimental data from Lamb et al. (2010) and a mixing coefficient $\gamma = 0.2$ is presented for reference.

simulation (averaged over time between $3,000 \leq t \leq 5{,}000$) and the experimental data of Lamb et al. (2010) and corresponding channel depth are plotted in Figure 8 (left) versus the characteristic Froude number. The authors in Singh and Shah (1971) showed experimentally and analytically that it was possible to express the height at the plunge point H_p as a function of the Froude number to the power of 2/3. It is possible to fit the present data and the experimental data of Lamb et al. (2010) with the function $a + bFr^{2/3}$. For the plunge position x_p results, the coefficients are $a = 63$ and $b = 22.2$, while for the height at the plunge point H_p, the coefficients are $a = 4.14$, and $b = 1.11$. The coefficient of determination is equal to $R^2 = 85.53\%$, which is very reasonable considering that experimental and numerical results were combined in order to make the fitting. The coefficients a and b are affected by changes in particle composition and grain-size distribution, declivity, roughness at the bottom of the channel, and outflow boundary condition. Overall, the agreement is very good with the model of Singh and Shah (1971), which means that the streamwise location of the plunging point and associated height can be estimated with the Froude number.

Akiyama and Stefan (1984) proposed a model for the prediction of the necessary depth for the plunging phenomenon to happen. The idea is to rearrange equation (2b) as follows:

$$\tilde{H}_p = \left(\frac{\tilde{q}_p^2}{R\tilde{c}_p \tilde{g} Fr_p^2} \right)^{1/3}, \tag{11}$$

where $\tilde{q}_p$, $\tilde{c}_p$, and Fr_p represent the flow discharge, total concentration, and Froude number at the plunge point, respectively, the last one being the key point of this analysis. Parker and Toniolo (2007) showed that it is possible to predict values for the Froude number at the plunge position Fr_p and just downstream of the plunge position Fr_d as a function of only a mixing coefficient defined as $\gamma = \frac{q_d}{q_0} - 1$.

The present turbulence-resolving simulations can be used to test these analytical models. For this analysis, the data for the flow rate and concentration obtained as function of x_1 are computed with a time average (for $3,000 \leq t \leq 5,000$), a spatial average in the direction x_3, and with an integration in vertical direction. The authors in Lamb et al. (2010) mentioned that a value of $\gamma \approx 0.2$ is reasonable for entrainment up to a distance downstream of the plunge point for which the depth is five time the depth at the plunge point. They also stated that the continuous entrainment at the interface between the underflow current and the ambient fluid will cause γ to increase so the model of Parker and Toniolo (2007) would not be valid in the underflow region illustrated in Figure 2. The proposed coefficient mixing value is recovered in the present simulations, as showed in Figure 8 (right). The numerical data for the four cases are very close to each other. The significant scatter in the experimental data was interpreted as a result from the error in calculating the discharge with no possible measurement in the upper $\sim 4h$ of the water column (Lamb et al., 2010).

The model analysis of Parker and Toniolo (2007) is giving a depth ratio of $H_d = 0.7H_p$ for $\gamma = 0.2$, with a Froude number at the plunge position equal to $Fr_d = 1.1$ and a Froude number downstream of the plunge point equal to $Fr_p = 0.45$. In the present simulations, the flow height downstream of the plunge point H_p is calculated as the distance from the bottom floor to the elevation profile. The results presented in Figure 9 (left)

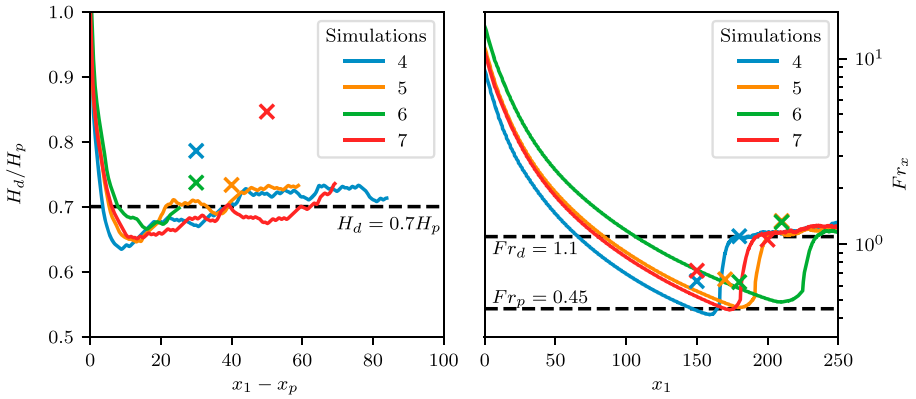

Figure 9. (left) The ratio between flow height at plunge point H_p and downstream plunge point H_d as function of x_1. Points represent experimental data from Lamb et al. (2010), and the depth ratio $H_d = 0.7H_p$ is predicted by Parker and Toniolo (2007) for $\gamma = 0.2$. (right) Local Froude number, computed using equation (2b), as a function of x_1. The points represent the experimental data from Lamb et al. (2010).

are showing the abrupt height reduction in the plunge zone. It can also be seen that within about 20*h*, the simulated flow height is reasonably close to the evaluated value, with a much better agreement by comparison to the experimental data. The four simulations are showing the same trend, whereas experiments are more scattered. Figure 9 (right) shows the evolution of the local Froude number Fr_x as a function of the streamwise distance x_1, making it evident that the Froude number continuously decreases in the depth-limited plume while the depth is increasing and the particle sedimentation is affecting the suspended concentration, even upstream of the plunge point. At the plunge point, the confined flow transitions from the lowest Froude number $Fr_p = 0.45$ to a quasi-constant value of 1.1 for the underflow density current. Both values are in good agreement with published experimental and theoretical analyses. As already mentioned in section 1, in a more general framework, the quasi steady state Froude number depends on the bed slope, and, to a minor degree, to the bed roughness and the size of the suspended sediment (Sequeiros, 2012).

6. Conclusions

Polydisperse particles turbulence-resolving simulations (implicit LES approach) were performed to study the plunge phenomenon in hyperpycnal flows flowing at the bottom floor of a tilted channel. Comparisons were made with the experimental data of Lamb et al. (2010) and the analytical models of Parker and Toniolo (2007), and a good agreement was found with the reference data. The main advantage of using turbulence-resolving simulations as opposed to experiments is that it is possible to access all the quantities of the flow at all time and everywhere in the test section. The proposed numerical framework has been validated, and very accurate simulations can now be used to investigate in more details the influence of various parameters such as the angle of the titled channel or to get more information about the mixing process occurring at the interface between the underflow density current and the ambient fluid. The correct reproduction of the turbulence structures in the plunge region is crucially needed to design more accurate models, and this can only be achieved with 3-D turbulence-resolving simulations. The vast majority of the analytical and empirical models are based on assumptions (steady uniform flow, uniform velocity profiles, constant density for the ambient fluid, and no mixing), which might not be relevant in real conditions. A big challenge is related to a better understanding of the entrainment at the interface between the ambient fluid and the underflow density current: how to discriminate between the engulfment and nibbling mechanisms? The 3-D turbulence-resolving simulations will certainly help to address this challenge, for example, by trying to quantify the volume of fluid that becomes rotational at the interface. Another feature that could be important for a better understanding of the plunge phenomenon is the entrainment of bed sediment. However, this would only be possible by modeling individual particles as opposed to a concentration (Ji et al., 2013). Future studies will be performed with a longer and deeper computational domain in order to better stabilize the plunge position. An open basin setup, more representative of real situations than a channelized setup, will also be considered following the recent work of Francisco et al. (2018) for finite-release particle-laden gravity currents. In most lakes and reservoirs, the variation of the inlet cross section is three-dimensional, with both the depth and width increasing with distance so it is important to be able to reproduce this feature in future studies.

Acknowledgments
This research was supported by Petrobras S.A. and CAPES. All simulations were performed on the high-performance facility LAD-PUCRS at the Pontifícia Universidade Católica do Rio Grande do Sul, Porto Alegre, Rio Grande do Sul, Brazil. The data are available at https://imperialcollegelondon.app.box.com/s/hy6v4uj8e3o47eu26vgmoh5uxe17xsx7. The flow solver `Incompact3d` can be obtained at https://github.com/xcompact3d.

References

Akiyama, J., & Stefan, H. G. (1984). Plunging flow into a reservoir: Theory. *Journal of Hydraulic Engineering*, *110*(4), 484–499.
Alavian, V. (1986). Behavior of density currents on an incline. *Journal of Hydraulic Engineering*, *112*(1), 27–42.
Alavian, V., Jirka, G. H., Denton, R. a., Johnson, M. C., & Stefan, H. G. (1992). Density currents entering lakes and reservoirs. *Journal of Hydraulic Engineering*, *118*(11), 1464–1489.
Bournet, P., Dartus, D., Tassin, B., & Vincon-Leite, B. (1999). Numerical investigation of plunging density current. *Journal of Hydraulic Engineering*, *125*(6), 584–594.
da Silva, C. B., Hunt, J. C., Eames, I., & Westerweel, J. (2014). Interfacial layers between regions of different turbulence intensity. *Annual Review of Fluid Mechanics*, *46*, 567–590.
Dai, A., Cantero, M. I., & García, M. H. (2007). Plunging of two-dimensional gravity currents. In *Proc., 5th Int. Symp. on Environmental Hydraulics*, IAHR, Temp, Ariz.
Dai, A., & García, M. H. (2009). Discussion of "Note on the Analysis of Plunging of Density Flows" by Gary Parker and Horacio Toniolo. *Journal of Hydraulic Engineering*, *135*(6), 532–533.
Dairay, T., Lamballais, E., Laizet, S., & Vassilicos, J. C. (2017). Numerical dissipation vs. subgrid-scale modelling for large eddy simulation. *Journal of Computational Physics*, *337*, 252–274.
Dallimore, C. J., Imberger, J., & Hodges, B. R. (2004). Modeling a plunging underflow. *Journal of Hydraulic Engineering*, *130*(11), 1068–1076.
Farrell, G. J., & Stefan, H. G. (1988). Mathematical modeling of plunging reservoir flows. *Journal of Hydraulic Research*, *26*(5), 525–537.
Francisco, E., Espath, L., Laizet, S., & Silvestrini, J. (2018). Reynolds number and settling velocity influence for finite-release particle-laden gravity currents in a basin. *Computers & Geosciences*, *110*, 1–9.
Garcia, M. H. (1994). Depositional turbidity currents laden with poorly sorted sediment. *Journal of Hydraulic Engineering*, *120*(11), 1240–1263.
Gautier, R., Laizet, S., & Lamballais, E. (2014). A DNS study of jet control with microjets using an immersed boundary method. *International Journal of Computational Fluid Dynamics*, *28*(6-10), 393–410.
Grinstein, F. F., Margolin, L. G., & Rider, W. J. (2007). *Implicit large eddy simulation: Computing turbulent fluid dynamics*. Cambridge: Cambridge University Press.
Haller, G. (2005). An objective definition of a vortex. *Journal of Fluid Mechanics*, *525*, 1–26.
Horner-Devine, A. R., Hetland, R. D., & MacDonald, D. G. (2015). Mixing and transport in coastal river plumes. *Annual Review of Fluid Mechanics*, *47*, 569–594.
Ji, C., Munjiza, A., Avital, E., Ma, J., & Williams, J. (2013). Direct numerical simulation of sediment entrainment in turbulent channel flow. *Physics of Fluids*, *25*(5), 056601.
Julien, P. (2010). *Erosion and sedimentation*. Cambridge: Cambridge University Press.
Kassem, A., & Imran, J. (2001). Simulation of turbid underflows generated by the plunging of a river. *Geology*, *29*(7), 655–658.
Kassem, A., Imran, J., & Khan, J. A. (2003). Three-dimensional modeling of negatively buoyant flow in diverging channels. *Journal of Hydraulic Engineering*, *129*(12), 936–947.
Khan, S. M., Imran, J., Bradford, S., & Syvitski, J. (2005). Numerical modeling of hyperpycnal plume. *Marine Geology*, *222*, 193–211.
Laizet, S., & Lamballais, E. (2009). High-order compact schemes for incompressible flows: A simple and efficient method with quasi-spectral accuracy. *Journal of Computational Physics*, *228*(16), 5989–6015.
Laizet, S., & Li, N. (2011). Incompact3d: A powerful tool to tackle turbulence problems with up to O(10^5) computational cores. *International Journal for Numerical Methods in Fluids*, *67*(11), 1735–1757.
Lamb, M. P., McElroy, B., Kopriva, B., Shaw, J., & Mohrig, D. (2010). Linking river-flood dynamics to hyperpycnal-plume deposits: Experiments, theory, and geological implications. *Geological Society of America Bulletin*, *122*(9-10), 1389–1400.
Lamb, M. P., & Mohrig, D. (2009). Do hyperpycnal-flow deposits record river-flood dynamics? *Geology*, *37*(12), 1067–1070.
Lamballais, E., Fortuné, V., & Laizet, S. (2011). Straightforward high-order numerical dissipation via the viscous term for direct and large eddy simulation. *Journal of Computational Physics*, *230*(9), 3270–3275.
Launder, B. E., & Spalding, D. B. (1972). *Mathematical models of turbulence*. Cambridge, MA: Academic Press.
Lee, H.-Y., & Yu, W.-S. (1997). Experimental study of reservoir turbidity current. *Journal of Hydraulic Engineering*, *123*(6), 520–528.
Lele, S. K. (1992). Compact finite difference schemes with spectral-like resolution. *Journal of Computational Physics*, *103*(1), 16–42.
McCool, W. W., & Parsons, J. D. (2004). Sedimentation from buoyant fine-grained suspensions. *Continental Shelf Research*, *24*(10), 1129–1142.
Meiburg, E., & Kneller, B. (2010). Turbidity currents and their deposits. *Annual Review of Fluid Mechanics*, *42*, 135–156.
Mulder, T., Syvitski, J. P. M., Migeon, S., Faugeres, J.-C., & Savoye, B. (2003). Marine hyperpycnal flows: Initiation, behavior and related deposits. A review. *Marine and Petroleum Geology*, *20*(6), 861–882.
Nasr-Azadani, M. M., Hall, B., & Meiburg, E. (2013). Polydisperse turbidity currents propagating over complex topography: Comparison of experimental and depth-resolved simulation results. *Computers and Geosciences*, *53*(1998), 141–153.
Necker, F., Härtel, C., Kleiser, L., & Meiburg, E. (2002). High-resolution simulations of particle-driven gravity currents. *International Journal of Multiphase Flow*, *28*(2), 279–300.
Parker, G., & Toniolo, H. (2007). Note on the analysis of plunging of density flows. *Journal of Hydraulic Engineering*, *133*(6), 690–694.
Sagaut, P. (2006). *Large eddy simulation for incompressible flows: An introduction*. Berlin, Germany: Springer Science & Business Media.
Savage, S., & Brimberg, J. (1975). Analysis of plunging phenomena in water reservoirs. *Journal of Hydraulic Research*, *13*(2), 187–205.
Sequeiros, O. E. (2012). Estimating turbidity current conditions from channel morphology: A Froude number approach. *Journal of Geophysical Research*, *117*, C04003. https://doi.org/10.1029/2011JC007201
Sequeiros, O. E., Naruse, H., Endo, N., Garcia, M. H., & Parker, G. (2009). Experimental study on self-accelerating turbidity currents. *Journal of Geophysical Research*, *114*, C05025. https://doi.org/10.1029/2008JC005149
Singh, B., & Shah, C. (1971). Plunging phenomenon of density currents in reservoirs. *La Houille Blanche*, *1*, 59–64.
Trenberth, K. E., Smith, L., Qian, T., Dai, A., & Fasullo, J. (2007). Estimates of the global water budget and its annual cycle using observational and model data. *Journal of Hydrometeorology*, *8*(4), 758–769.
Üneş, F. (2008). Analysis of plunging phenomenon in dam reservoirs using three-dimensional density flow simulations. *Canadian Journal of Civil Engineering*, *35*(10), 1138–1151.
Üneş, F. (2010). Prediction of density flow plunging depth in dam reservoirs: An artificial neural network approach. *Clean–Soil, Air, Water*, *38*(3), 296–308.